Astronomy
&
Astrophysics

Observations of water with *Herschel*/HIFI toward the high-mass protostar AFGL 2591[⋆]

Y. Choi[1,2], F. F. S. van der Tak[2,1], E. F. van Dishoeck[3,4], F. Herpin[5,6], and F. Wyrowski[7]

[1] Kapteyn Astronomical Institute, University of Groningen, PO Box 800, 9700 AV Groningen, The Netherlands
e-mail: y.choi@astro.rug.nl
[2] SRON Netherlands Institute for Space Research, PO Box 800, 9700 AV Groningen, The Netherlands
[3] Leiden Observatory, Leiden University, PO Box 9513, 2300 RA Leiden, The Netherlands
[4] Max-Planck Institut für Extraterrestrische Physik, Giessenbachstrasse 1, 85748 Garching, Germany
[5] Université de Bordeaux, Observatoire Aquitain des Sciences de l'Univers, 2 rue de l'Observatoire, BP 89, 33270 Floirac Cedex, France
[6] CNRS, LAB, UMR 5804, Laboratoire d'Astrophysique de Bordeaux, 2 rue de l'Observatoire, BP 89, 33270 Floirac Cedex, France
[7] Max-Planck Institut für Radioastronomie, Auf dem Hügel 69, 53121 Bonn, Germany

ABSTRACT

Context. Water is an important chemical species in the process of star formation, and a sensitive tracer of physical conditions in star-forming regions because of its rich line spectrum and large abundance variations between hot and cold regions.
Aims. We use spectrally resolved observations of rotational lines of H_2O and its isotopologs to constrain the physical conditions of the water emitting region toward the high-mass protostar AFGL 2591.
Methods. *Herschel*/HIFI spectra from 552 up to 1669 GHz show emission and absorption in 14 lines of H_2O, $H_2^{18}O$, and $H_2^{17}O$. We decompose the line profiles into contributions from the protostellar envelope, the bipolar outflow, and a foreground cloud. We use analytical estimates and rotation diagrams to estimate excitation temperatures and column densities of H_2O in these components. Furthermore, we use the non-local thermodynamic equilibrium (LTE) radiative transfer code RADEX to estimate the temperature and volume density of the H_2O emitting gas.
Results. Assuming LTE, we estimate an excitation temperature of ~42 K and a column density of ~2×10^{14} cm^{-2} for the envelope and ~45 K and 4×10^{13} cm^{-2} for the outflow, in beams of 4″ and 30″, respectively. Non-LTE models indicate a kinetic temperature of ~60−230 K and a volume density of 7×10^6−10^8 cm^{-3} for the envelope, and a kinetic temperature of ~70−90 K and a gas density of ~10^7−10^8 cm^{-3} for the outflow. The ortho/para ratio of the narrow cold foreground absorption is lower than three (~1.9 ± 0.4), suggesting a low temperature. In contrast, the ortho/para ratio seen in absorption by the outflow is about 3.5 ± 1.0, as expected for warm gas.
Conclusions. The water abundance in the outer envelope of AFGL 2591 is ~10^{-9} for a source size of 4″, similar to the low values found for other high-mass and low-mass protostars, suggesting that this abundance is constant during the embedded phase of high-mass star formation. The water abundance in the outflow is ~10^{-10} for a source size of 30″, which is ~10× lower than in the envelope and in the outflows of high-mass and low-mass protostars. Since beam size effects can only increase this estimate by a factor of 2, we suggest that the water in the AFGL 2591 outflow is affected by dissociating UV radiation as a result of the low extinction in the outflow lobe.

Key words. ISM: molecules – ISM: abundances – ISM: individual objects: AFGL 2591 – stars: formation

1. Introduction

Massive stars play a major role in the interstellar energy budget and the shaping of the galactic environment. However, the formation of high-mass stars is not well understood for several reasons: they are rare, they have a short evolution time scale, they are born deeply embedded, and they are far from us. The water molecule is thought to be a sensitive tracer of physical conditions and dynamics in star-forming regions because of its large abundance variations between hot and cold regions. Water is also an important reservoir of oxygen and therefore a crucial ingredient in the chemistry of oxygen-bearing molecules. In the surroundings of embedded protostars, water can be formed by three different mechanisms (see van Dishoeck et al. 2013, for a review).

First, in molecular clouds, water may be formed in the gas phase by ion-molecule chemistry through dissociative recombination of H_3O^+. Second, in cold and dense cores, on the surfaces of cold dust grains, O and H atoms may combine to form water-rich ice mantles. These mantles will evaporate when the grains are heated to ~100 K by protostellar radiation or sputtered by outflow shocks. Third, in gas with temperatures above 300 K, reactions of O and OH with H_2 drive all gas-phase oxygen into water. Such high temperatures may occur very close to the stars, or near outflow shocks. Therefore, measurement of the water abundance is a step towards understanding the star formation process.

AFGL 2591 is a well studied high-mass star-forming region at a distance of 3.3 kpc (Rygl et al. 2012). The source is one of the rare cases of a massive star-forming region in relative isolation so that we can study physical parameters like density, temperature, and velocity structure without confusion from other

Table 1. Observed lines.

Molecule	Transition	Obsid	ν (GHz)	E_{up} (K)	T_{sys} (K)	t_{int} (min)	Beam (″)	η_{mb}	δv (MHz)	rms (mK)
o-H$_2^{18}$O^a	$1_{10}-1_{01}$	1342210763	547.676	60.5	74	33	38.7	0.75	0.48	14
o-H$_2^{17}$O	$1_{10}-1_{01}$	1342192360	552.020	61.0	72	2.2	38.0	0.75	0.48	33
o-H$_2$O^a	$1_{10}-1_{01}$	1342210763	556.936	61.0	74	33	38.0	0.75	0.24	14
p-H$_2$O	$2_{11}-2_{02}$	1342192335	752.033	136.9	178	3.9	28.2	0.75	0.24	83
p-H$_2$O	$2_{02}-1_{11}$	1342195019	987.926	100.8	371	6.3	21.3	0.74	0.24	115
p-H$_2^{18}$O	$2_{02}-1_{11}$	1342195020	994.675	100.8	276	7.8	21.3	0.74	0.48	66
o-H$_2^{18}$O	$3_{12}-3_{03}$	1342194796	1095.627	249.4	373	27	19.2	0.74	0.48	51
o-H$_2$O	$3_{12}-3_{03}$	1342194796	1097.365	249.4	373	27	19.2	0.74	0.24	51
p-H$_2^{18}$O	$1_{11}-0_{00}$	1342194795, 1342197973	1101.698	53.4	350	56	19.2	0.74	0.48	33
p-H$_2^{17}$O	$1_{11}-0_{00}$	1342194796	1107.166	53.4	373	27	19.1	0.74	0.48	42
p-H$_2$O	$1_{11}-0_{00}$	1342194795, 1342197973	1113.343	53.4	390	57	19.0	0.74	1.1	33
o-H$_2$O	$2_{21}-2_{12}$	1342192570	1661.007	194.1	1416	16	12.8	0.71	1.1	166
o-H$_2^{17}$O	$2_{12}-1_{01}$	1342192570	1662.464	113.6	1417	17	12.8	0.71	1.1	103
o-H$_2$O	$2_{12}-1_{01}$	1342192570	1669.904	114.4	1417	17	12.7	0.71	1.1	95

Notes. $^{(a)}$ This line was mapped in OTF mode.

nearby objects even with single-dish telescopes. Large amounts of gas and dust toward this source block our view at optical wavelengths, but result in bright infrared emission. This source is also associated with a weak radio continuum source and with a bipolar outflow. There is very high velocity CO mid-infrared absorption (Mitchell et al. 1989). The luminosity of this source is about 2.0×10^5 $L_\odot$ (Sanna et al. 2012).

AFGL 2591 has been observed in water lines over a range of excitation conditions. Helmich et al. (1996) found more than 30 lines within the bending vibration of water between 5.5 and 6.6 μm using ISO-SWS. No lines of H$_2^{18}$O or vibrationally-excited H$_2$O were seen. The ISO data indicate a high excitation temperature (>200 K) and a high abundance ($\sim 2-6 \times 10^{-5}$). Boonman et al. (2003) observed gas-phase H$_2$O lines between 5 and 540 μm with ISO and SWAS. They found that ice evaporation in the warm inner envelope and freeze-out in the cold outer part together with pure gas-phase chemistry reproduces the H$_2$O observations. However, these conclusions were based on spectrally unresolved data that could not separate envelope and outflow. van der Tak et al. (2006) and Wang et al. (2012) presented ground-based observations of H$_2^{18}$O toward AFGL 2591 with the Plateau de Bure Interferometer, which have high resolution but are limited to a single line. These data confirm the abundance jump inferred from the ISO/SWAS data, and suggest the presence of a circumstellar disk.

This paper uses *Herschel*/HIFI observations of water lines toward AFGL 2591 to learn about physical processes in this region and measure the abundance of water in its various physical components as a step towards understanding the process of high-mass star formation. With its much higher spatial and spectral resolution and higher sensitivity than previous space missions, *Herschel*/HIFI is able to resolve the line profiles and detect isotopic lines, providing essential information on the physical and chemical structure of the region.

Our observations of AFGL 2591 are summarized in Sect. 2. In Sect. 3 we show the observational results and simple analysis. Section 4 presents the analysis of physical conditions using observational data and radiative transfer modeling. Finally, we discuss our results in Sect. 5.

2. Observations

AFGL 2591 was observed with the Heterodyne Instrument for the Far-Infrared (HIFI; de Graauw et al. 2010) onboard ESA's *Herschel* Space Observatory (Pilbratt et al. 2010). These observations were conducted between March and June 2010, using the dual beam switch (DBS) mode as part of the guaranteed time key program Water In Star-forming regions with *Herschel* (WISH; van Dishoeck et al. 2011). The coordinates of the observed position in AFGL 2591 are 20^{h}29^{m}24^s.87 and +40°11′19.5″ (J2000).

Data were taken simultaneously in horizontal and vertical polarizations using both the correlator-based high-resolution spectrometer (HRS) and the acousto-optical wide-band spectrometer (WBS) with a 1.1 MHz resolution. We used the double beam switch observing mode with a throw of 3′. HIFI receivers are double sideband with a sideband ratio close to unity. Currently, the flux scale accuracy is estimated to be about 10% for bands 1 and 2, 15% for bands 3 and 4, and 20% in bands 6 and 7 (Roelfsema et al. 2012). We show the HRS spectra in Figs. 1 and 2, with the exception of the p-H$_2$O $1_{11}-0_{00}$, o-H$_2$O $2_{12}-1_{01}$, o-H$_2$O $2_{21}-2_{12}$, and o-H$_2^{17}$O $2_{12}-1_{01}$ lines, for which WBS spectra were used since the velocity range covered by the HRS was insufficient.

AFGL 2591 was also mapped with HIFI in OTF mode in the o-H$_2$O $1_{10}-1_{01}$, p-H$_2$O $1_{11}-0_{00}$, and p-H$_2$O $2_{02}-1_{11}$ lines. These observations were carried out between November and December 2010. We have taken the o-H$_2$O $1_{10}-1_{01}$ and o-H$_2^{18}$O $1_{10}-1_{01}$ lines from the central positions of the maps since we do not have data for these two lines using the double beam switch observing mode. A full analysis of these maps will be presented elsewhere.

The frequencies, energy of the upper levels, system temperatures, integration times, the beam size and efficiency, rms noise level at a given spectral resolution for each of the lines are provided in Table 1. The calibration of the data was performed in the *Herschel* interactive processing environment (HIPE; Ott 2010) version 8.0. The resulting Level 2 double sideband (DSB) spectra were exported to the FITS format for a subsequent
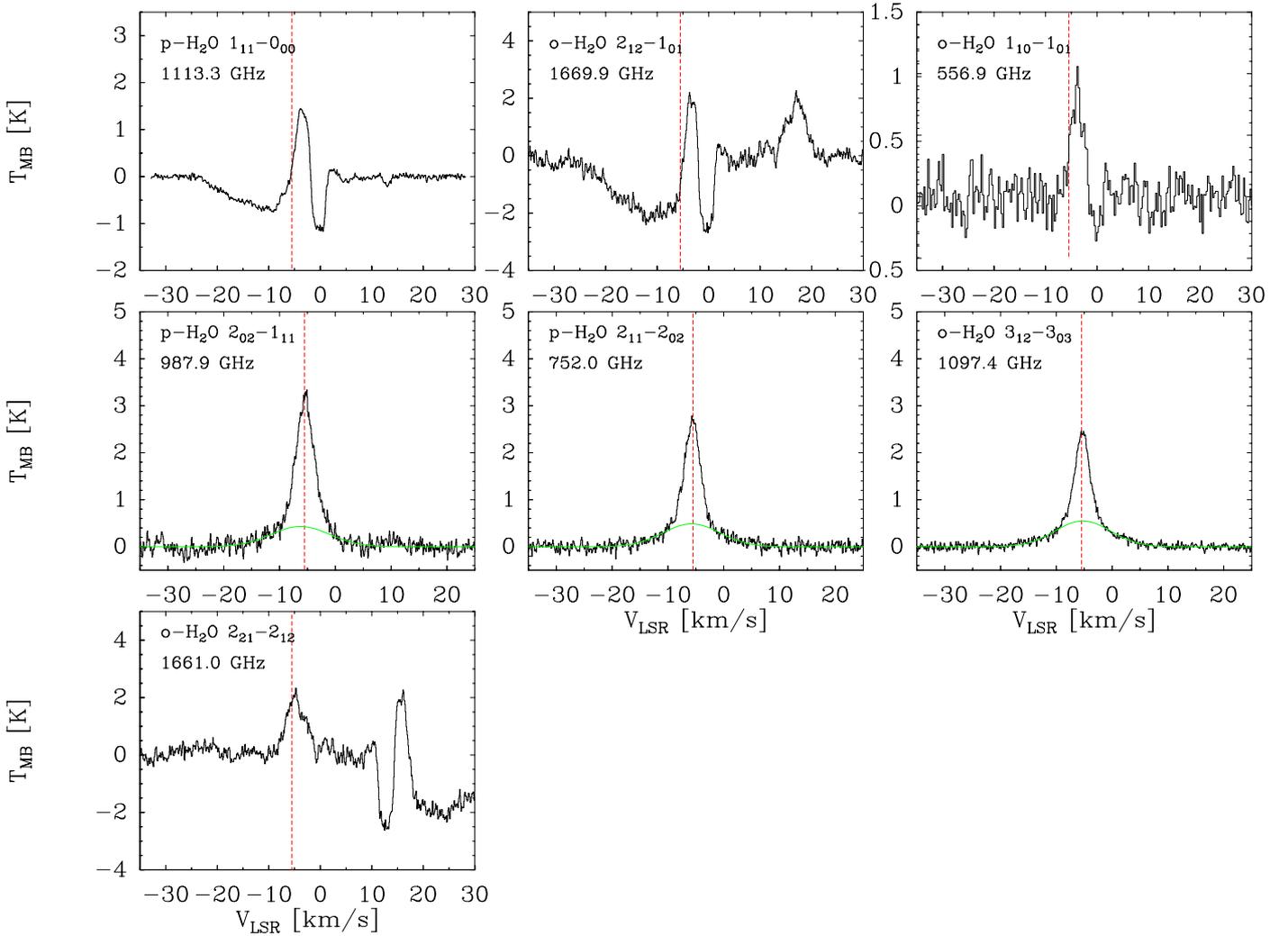
Fig. 1. Spectra of $H_2^{16}O$ lines toward the high-mass star-forming region AFGL 2591. Dashed red lines are drawn at the source velocity $V_{LSR} = -5.5$ km s^{-1}. Green lines present the outflow components. We note that the H_2O $2_{12}-1_{01}$ and $2_{21}-2_{12}$ lines occur in opposite sidebands of the same spectrum, causing the features near 20 km s^{-1}.

data reduction and analysis using the IRAM GILDAS[1] package. These lines are not expected to be polarized, thus, after inspection, data from the two polarizations were averaged together.

3. Results

The HIFI spectra of AFGL 2591 show strong emission and absorption by H_2O (Fig. 1), and weaker emission in $H_2^{18}O$ and $H_2^{17}O$ lines (Fig. 2). The line profiles differ considerably between the ground-state levels of H_2O, its excited levels, and its isotopologs.

The ground-state lines of the main isotopologue (p-H_2O $1_{11}-0_{00}$, o-H_2O $2_{12}-1_{01}$, o-H_2O $1_{10}-1_{01}$) show a mix of emission and absorption, as found before for DR21 (van der Tak et al. 2010) and W3 IRS5 (Chavarría et al 2010). First, all three lines show an emission feature of the source at $V_{LSR} = -3$ km s^{-1}, somewhat red-shifted with respect to the V_{LSR} of the source at $V_{LSR} = -5.5$ km s^{-1} (van der Tak et al. 1999). The emission feature seems to be related to an expansion of the outer envelope. The expansion is probably powered by

outflows which are known to exist in AFGL 2591 (Lada et al. 1984). The blue side of the emission is smooth because of the outflow, but the red side is sharply truncated because of absorption by a foreground cloud at ~0 km s^{-1}.

Second, a broad and asymmetric absorption component occurs near $V_{LSR} = -10$ km s^{-1} which from its shape has a likely origin in a wind. This broad absorption component is only detected in the p-H_2O $1_{11}-0_{00}$ and o-H_2O $2_{12}-1_{01}$ lines. We probably do not see it in the o-H_2O $1_{10}-1_{01}$ line because the signal-to-noise ratio on the continuum is not high enough.

Third, the ground-state H_2O line profiles show evidence for two foreground clouds. The narrow absorption component around $V_{LSR} = 0$ km s^{-1} is detected in all three lines, and corresponds to a cloud known from ground-based observations (van der Tak et al. 1999). A second, weaker absorption feature near $V_{LSR} = 13$ km s^{-1} is only seen in the p-H_2O $1_{11}-0_{00}$ line. The continuum at o-H_2O $1_{10}-1_{01}$ line is presumably too weak to see this feature, and the o-H_2O $2_{12}-1_{01}$ spectrum is blended with the o-H_2O $2_{21}-2_{12}$ line. This cloud is not known from ground-based observations, and is also seen in HF observations (Emprechtinger et al. 2012) but not in CO observations by *Herschel*/HIFI of this source (van der Wiel et al. 2013), so it is probably a diffuse cloud.

---

[1] http://www.iram.fr/IRAMFR/GILDAS/
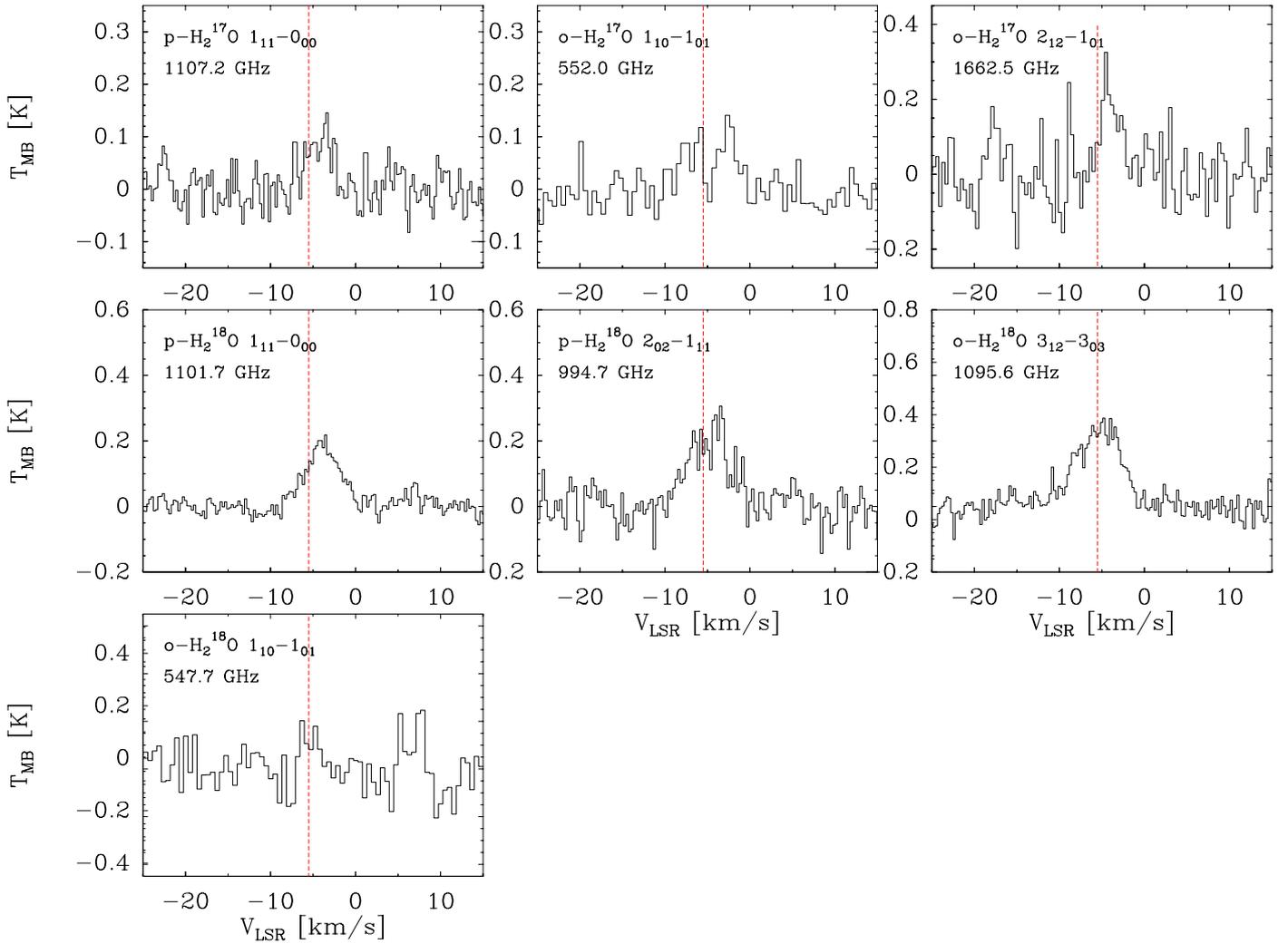
Fig. 2. Spectra of $H_2^{17}O$ and $H_2^{18}O$ lines toward the high-mass star-forming region AFGL 2591. Dashed lines are drawn at the source velocity $V_{LSR} = -5.5$ km s^{-1}.

The excited-state lines of H_2O (p-H_2O $2_{02}-1_{11}$, p-H_2O $2_{11}-2_{02}$, and o-H_2O $3_{12}-3_{03}$) appear purely in emission and show two velocity components. The components have Gaussian shapes, one being wider (*FWHM* = 11–12 km s^{-1}) than the other (*FWHM* = 3–4 km s^{-1}). Studies of low-mass protostars from the WISH program (Kristensen et al. 2010, 2012) refer to these components as the broad and narrow components, but we will call them the outflow and envelope components, after their likely physical origin. We assume that the broad component is due to the high-velocity outflow associated with the protostar seen in absorption in p-H_2O $1_{11}-0_{00}$ and o-H_2O $2_{12}-1_{01}$ lines, even though it covers a somewhat smaller velocity range. The narrow component is potentially associated with the protostellar envelope.

The lines of $H_2^{18}O$ and $H_2^{17}O$ appear purely in emission and are dominated by the envelope, centered around $V_{LSR} = -5$ km s^{-1}. In addition, the $H_2^{18}O$ lines around 1 THz may show a broadening due to a weak outflow component. Likewise, the high-frequency o-$H_2^{17}O$ $1_{10}-1_{01}$ line appears to be broader than the other two $H_2^{17}O$ lines.

We extracted line parameters from the observed profiles by fitting Gaussians; Table 2 gives the results for the emission lines and Table 3 for the absorption lines. For the emission features, we fitted the p-H_2O $2_{02}-1_{11}$, p-H_2O $2_{11}-2_{02}$, and

Table 2. Parameters of the H_2O, $H_2^{18}O$, and $H_2^{17}O$ emission line profiles obtained from Gaussian fits.

Molecule	Transition	$\int T_{MB} dV$ (K km s^{-1})	V_{LSR} (km s^{-1})	ΔV (km s^{-1})	T_{MB} (K)
p-H_2O	$2_{02}-1_{11}$	6.1 (0.5)	–6.3 (0.3)	10.1 (0.6)	0.6
		9.9 (0.5)	–5.4 (0.1)	3.7 (0.1)	2.5
p-H_2O	$2_{11}-2_{02}$	5.9 (0.2)	–5.8 (0.1)	11.1 (0.5)	0.5
		7.5 (0.2)	–5.6 (0.1)	3.3 (0.1)	2.1
o-H_2O	$3_{12}-3_{03}$	6.4 (0.1)	–5.3 (0.1)	10.6 (0.2)	0.6
		5.9 (0.1)	–5.3 (0.1)	3.1 (0.0)	1.8
p-$H_2^{18}O$	$1_{11}-0_{00}$	1.1 (0.1)	–4.0 (0.1)	5.0 (0.2)	0.2
p-$H_2^{18}O$	$2_{02}-1_{11}$	1.3 (0.1)	–4.8 (0.2)	5.5 (0.4)	0.2
o-$H_2^{18}O$	$3_{12}-3_{03}$	1.3 (0.1)	–5.2 (0.1)	5.6 (0.2)	0.2
p-$H_2^{17}O$	$1_{11}-0_{00}$	0.4 (0.1)	–4.3 (0.2)	3.8 (0.4)	0.1
o-$H_2^{17}O$	$1_{10}-1_{01}$	0.5 (0.1)	–4.2 (0.6)	7.7 (1.2)	0.1
o-$H_2^{17}O$	$2_{12}-1_{01}$	0.5 (0.1)	–4.2 (0.2)	2.3 (0.5)	0.2

o-H_2O $3_{12}-3_{03}$ line profiles assuming two velocity components, while the other emission lines are fitted as one velocity component. The $H_2^{18}O$ lines appear broader than the narrow emission components seen in H_2O (see Table 2), so that the profiles are probably a mixture of envelope and outflow emission seen at

Table 3. Column densities estimated from p-H_2O $1_{11}-0_{00}$, o-H_2O $2_{12}-1_{01}$, and o-H_2O $1_{10}-1_{01}$ absorption line profiles.

Line	T_{cont} (K)	Vel. range (km s^{-1})	τ^a	N (10^{12} cm^{-2})
p-H_2O $1_{11}-0_{00}$	1.1 ± 0.2	-24 to -5.5	0.5 ± 0.1	20.9 ± 4.4
		-2 to 1.5	1.6 ± 0.4	13.3 ± 2.8
		12 to 14	0.1 ± 0.1	0.4 ± 0.1
o-H_2O $2_{12}-1_{01}$	2.3 ± 0.5	-24 to -5.5	0.9 ± 0.2	73.8 ± 20.9
		-2 to 1.5	1.8 ± 0.5	38.9 ± 12.6
		12 to 14	$-$	$-$
o-H_2O $1_{10}-1_{01}$	0.1 ± 0.1	-24 to -5.5	$-$	$-$
		-2 to 1.5	0.5 ± 0.1	25.6 ± 3.6
		12 to 14	$-$	$-$

Notes. $^{(a)}$ τ is the velocity-averaged optical depth.

limited signal-to-noise ratio. The o-$H_2^{17}O$ $1_{10}-1_{01}$ might show two components but the signal-to-noise ratio is not good enough so that we assume that this line has one component.

4. Analysis

4.1. Absorption components

The ground-state lines of the main isotopologue (p-H_2O $1_{11}-0_{00}$, o-H_2O $2_{12}-1_{01}$, o-H_2O $1_{10}-1_{01}$) show three absorption components: 1) the broad $V_{LSR} = -10$ km s^{-1} component due to the molecular outflow; 2) the narrow $V_{LSR} = 0$ km s^{-1} component due to the known foreground cloud; and 3) the narrow $V_{LSR} = 13$ km s^{-1} component due to a new diffuse foreground cloud. We derived the optical depth in these three components using the expression

$$\tau = -\ln\left(\frac{T_{line}}{T_{cont}}\right), \tag{1}$$

where T_{cont} is the single side band (SSB) continuum intensity. This expression assumes that the sideband gain ratio is unity and that the continuum is completely covered by the absorbing layer. We applied a linear baseline fit in the vicinity of the absorption line to derive the continuum intensity at the absorption peak. Deriving the optical depth from the line-to-continuum ratio is based on the assumption that the excitation temperature is negligible with respect to the continuum temperature.

In the following analysis we assume that all water molecules are in the ortho and para ground states, so that the velocity integrated absorption is related to the molecular column density by

$$N = \frac{8\pi\nu^3 g_l}{c^3 A g_u} \int \tau dV, \tag{2}$$

where N is the column density, ν the frequency, c the speed of light, and τ is the optical depth. A stands for the Einstein-A coefficient and g_l and g_u are the degeneracy of the lower and the upper level of the transition. Subsequently, we integrated over the velocity ranges given in Table 3 to determine the column density for each component. The derived column densities and the optical depth of the three components are listed also in Table 3. For the velocity range from -24 km s^{-1} to -5.5 km s^{-1}, the column density is $\sim 2-7 \times 10^{13}$ cm^{-2} and the optical depth is $\sim 0.5-1$. On the other hand, the column density is $\sim 1-4 \times 10^{13}$ cm^{-2} and the averaged optical depth is $\sim 1.6-2$ for the velocity range from -2 km s^{-1} to 1.5 km s^{-1}.

More information about the physical conditions in the foreground clouds comes from the ortho-to-para ratio of H_2O. If this ratio is thermalized, it should rise from ~ 1 at low temperatures (~ 15 K) to ~ 3 at high temperatures (>40 K) as shown by Mumma et al. (1987). Since we have data for ortho- and para-H_2O, we can determine the ortho/para (o/p) ratio, although the dynamic range of the absorption data is limited by the signal-to-noise ratio on one hand and by saturation on the other.

For narrow component, we determine the o/p ratio using the ground state of the o-H_2O $1_{10}-1_{01}$ and the p-H_2O $1_{11}-0_{00}$ lines and we find a lower o/p ratio of $\sim 1.9 \pm 0.4$ in the narrow component, suggesting a lower temperature for the foreground cloud. On the other hand, for the broad component we do not see it in the o-H_2O $1_{10}-1_{01}$ line so we used the second ground state ortho-H_2O line, o-H_2O $2_{12}-1_{01}$ transition at 1670 GHz. The o/p ratio of the broad component is around three ($\sim 3.5 \pm 1.0$), which is reasonable because the gas in the outflow is probably warm as it is heated by shocks.

Similar results have been found for diffuse absorbing clouds toward continuum sources in the Galactic plane (Flagey et al. 2013). Their presented water o/p ratios were consistent with the high-temperature limit value of 3, with lower values for the clouds with the highest column densities. Presumably interstellar UV radiation does not fully penetrate those clouds, so that photo-electric heating of the gas is less efficient. Indeed, the total (ortho + para) H_2O column densities of the foreground clouds of AFGL 2591 are as high as $\sim 5 \times 10^{13}$ cm^{-2} assuming an o/p ratio of 3, similar to the values found for the clouds toward NGC 6334 I, which also have a similar o/p ratio of H_2O (Emprechtinger et al. 2010).

4.2. Emission components

To estimate the column densities and rotation temperatures of water in the envelope and outflow of AFGL 2591, we construct rotation diagrams for the $H_2^{17}O$ and $H_2^{18}O$ lines for the envelope and for the broad component of the p-H_2O $2_{02}-1_{11}$, p-H_2O $2_{11}-2_{02}$, and o-H_2O $3_{12}-3_{03}$ lines for the outflow. We assume an $^{16}O/^{18}O$ ratio of 550 and an $^{18}O/^{17}O$ ratio of 4 (Wilson & Rood 1994), and that the $H_2^{17}O$ and $H_2^{18}O$ lines have the same excitation temperature.

First, we assume that (1) the lines are optically thin; (2) the emission fills the telescope beam; and (3) all level populations can be characterized by a single excitation temperature T_{rot} and use following equations. The column densities of the molecules in the upper level N_u are related to the measured integrated intensities, $\int T_{mb} dV$ (Linke et al. 1979; Blake et al. 1984, 1987; Helmich et al. 1994) by

$$N_u/g_u = \frac{N_{tot}}{Q(T_{rot})} e^{-E_u/T_{rot}} = \frac{1.67 \times 10^{14}}{\nu \mu^2 S} \int T_{mb} dV, \tag{3}$$

where μ is the permanent dipole moment, N_{tot} is the total column density, $Q(T_{rot})$ is the partition function for the rotation temperature T_{rot}, and S is the line strength value. Thus, a logarithmic plot of the quantity on the right-hand side of equation as a function of E_u provides a straight line with slope $1/T_{rot}$ and intercept $N_{tot}/Q(T_{rot})$.

To test our assumption of low optical depth in the above analysis, we carry out a simple estimate of the line optical depths comparing the observed $H_2^{16}O$-to-$H_2^{18}O$ and $H_2^{18}O$-to-$H_2^{17}O$ line ratios to the isotopic ratios, based on the assumption that the excitation temperatures of the corresponding transitions is the same across isotopologues. The measured peak intensity ratios
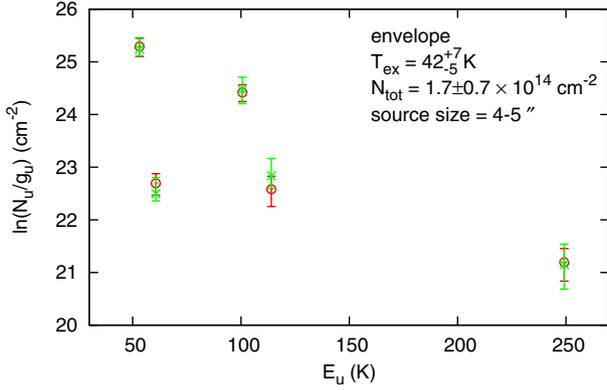
Fig. 3. Rotation diagram for the $H_2^{18}O$ and $H_2^{17}O$ emission components (envelope). Red open circles are the data observed with *Herschel*/HIFI. The green crosses represent the best-fit model from the population diagram analysis.

Fig. 4. Rotation diagram for the broad emission components seen in p-H_2O $2_{02}-1_{11}$, p-H_2O $2_{11}-2_{02}$, and o-H_2O $3_{12}-3_{03}$ (outflow). Red open circles are the data observed with *Herschel*/HIFI. The green crosses represent the best-fit model from the population diagram analysis.

of the p-$H_2^{16}O$ $2_{02}-1_{11}$-to-p-$H_2^{18}O$ $2_{02}-1_{11}$ and o-$H_2^{16}O$ $3_{12}-3_{03}$-to-p-$H_2^{18}O$ $3_{12}-3_{03}$ lines are 14 and 10, respectively, which is well below the isotopic ratio and indicates an optical depth of 3.6–3.9 for $H_2^{16}O$. In contrast, our observed p-$H_2^{18}O$ $1_{11}-0_{00}$-to-p-$H_2^{17}O$ $1_{11}-0_{00}$ line ratio is ~2, close to the isotopic ratio, which means that the optical depth of the $H_2^{18}O$ lines is $\lesssim 1$.

We now construct rotation diagrams which take into account the effect of optical depth. We define the optical depth correction factor C_τ (= $\tau/(1-e^{-\tau})$). If the source does not fill the beam, then the correct upper level column density is greater than that obtained assuming the beam to be filled by a factor equal to the beam dilution $f(=\Delta\Omega_a/\Delta\Omega_s)$, with Ω_s the size of the emission region and Ω_a the size of the telescope beam. The equation mentioned for the rotation diagram method as Eq. (3) can be modified to include the effect of optical depth τ through the factor C_τ and beam dilution f (Goldsmith & Langer 1999):

$$\ln\left(\frac{N_u}{g_u}\right) = \ln\left(\frac{N_{tot,thin}}{Q(T_{rot})}\right) - \frac{E_u}{kT_{ex}} - \ln(C_\tau) + \ln(f). \quad (4)$$

According to Eq. (4), for a given upper level, N_u can be evaluated from a set of $N_{tot,thin}$, T_{ex}, f and C_τ. Since C_τ is a function of $N_{tot,thin}$ and T_{ex}, the independent parameters are therefore $N_{tot,thin}$, T_{ex} and f, for which we solve self-consistently. A χ^2 minimization gives best-fit values of $N_{tot,thin}$, T_{ex}, and source sizes. In Figs. 3 and 4, rotation diagrams for water molecules in AFGL 2591 are presented. Red open circles are the data observed with *Herschel*/HIFI and the green crosses represent the best-fit model from population diagram analysis (using Eq. (4)).

Figure 3 shows the rotation diagram for $H_2^{18}O$ and $H_2^{17}O$, which is associated with the envelope. We construct rotation diagram for the envelope using five $H_2^{18}O$ and $H_2^{17}O$ emission lines because we do not detect the o-$H_2^{18}O$ $1_{10}-1_{01}$ line and p-$H_2^{18}O$ $1_{11}-0_{00}$ line and p-$H_2^{17}O$ $1_{11}-0_{00}$ line have the same energy of the upper level so we use the p-$H_2^{17}O$ $1_{11}-0_{00}$ line which is optically thin. The excitation temperature is estimated to be 42 ± 7 K with column density of $(1.7 \pm 0.7) \times 10^{14}$ cm^{-2} distributed over a ~4″ region. Line opacities of all the transitions used are estimated to be less than 14, which are consistent with those derived from the observed $H_2^{16}O$-to-$H_2^{18}O$ line ratios to the isotopic ratios.

Figure 4 presents the same analysis for the broad components seen in p-H_2O $2_{02}-1_{11}$, p-H_2O $2_{11}-2_{02}$, and o-H_2O $3_{12}-3_{03}$. The broad component is likely related to the
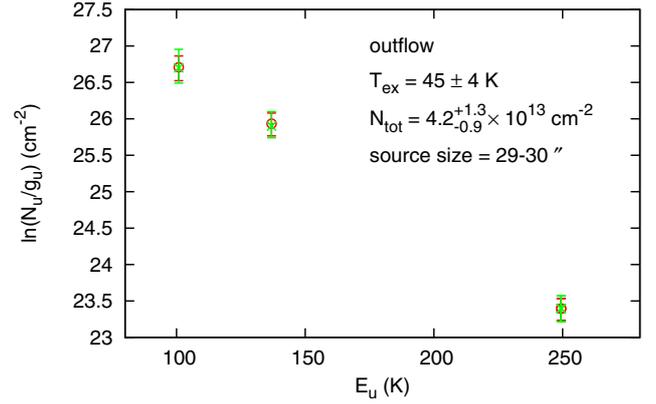
outflow, for which we find an excitation temperature of 45 ± 4 K, a column density of $(4.2 \pm 1.0) \times 10^{13}$ cm^{-2}, a source size of ~30″ and line opacities of the three H_2O transitions (broad components) used of <0.03.

4.3. Non-LTE calculations

We carried out non-local thermodynamic equilibrium (LTE) models of H_2O using the RADEX code (van der Tak et al. 2007) and state-of-the-art quantum mechanical collision rates of para and ortho H_2O with para and ortho H_2 (Daniel et al. 2011) as provided at the LAMDA database (Schöier et al. 2005). The same collision data are used for all isotopologs. To constrain the H_2O excitation, we generated a grid of models with values of T_{kin} between 10 and 1000 K, values of $n(H_2)$ from 10^3 to 10^9 cm^{-3}, and fixed the background radiation temperature at 2.73 K. The line width was fixed at 3 km s^{-1} for the envelope and 10.5 km s^{-1} for the outflow, and we applied a molecular column density of $N(H_2O) = 1 \times 10^{14}$ cm^{-2} and $N(H_2O) = 5 \times 10^{13}$ cm^{-2} for the envelope and the outflow, respectively. These molecular column densities are derived by the rotation diagram method (LTE) assuming source sizes of 4″ and 30″.

In the comparison with data, we first focus on the p-$H_2^{18}O$ $1_{11}-0_{00}$ and p-$H_2^{18}O$ $2_{02}-1_{11}$ lines for the envelope, which lie close in frequency, so that the effects of beam filling cancel out to first order. For the outflow, we use the p-H_2O $2_{11}-2_{02}$ and p-H_2O $2_{02}-1_{11}$ lines, based on the calculations of the p-H_2O $2_{11}-2_{02}$/p-H_2O $2_{02}-1_{11}$ line ratio, which traces both the gas temperature and density (Fig. A.1).

Figure 5 presents the calculated excitation temperatures of the p-$H_2^{18}O$ $1_{11}-0_{00}$ and p-$H_2^{18}O$ $2_{02}-1_{11}$ lines for the envelope (upper) and of the p-H_2O $2_{11}-2_{02}$ and p-H_2O $2_{02}-1_{11}$ lines for the outflow (lower), as a function of gas density and kinetic temperature. The calculations show that the derived range of excitation temperatures for the envelope (gray area in upper panels) based on the rotation diagram method (LTE) indicates a gas density of $7\times10^6-10^8$ cm^{-3} and a kinetic temperature of ~60−230 K indicating subthermal excitation. On the other hand, the models indicate that a gas density of ~10^7-10^8 cm^{-3} and a kinetic temperature of ~70−90 K reproduce the observations of the outflow (gray area in lower panels).

To compare LTE and non-LTE calculations, we construct the rotation diagrams for the broad components of the p-H_2O $2_{02}-1_{11}$, p-H_2O $2_{11}-2_{02}$, and o-H_2O $3_{12}-3_{03}$ lines using
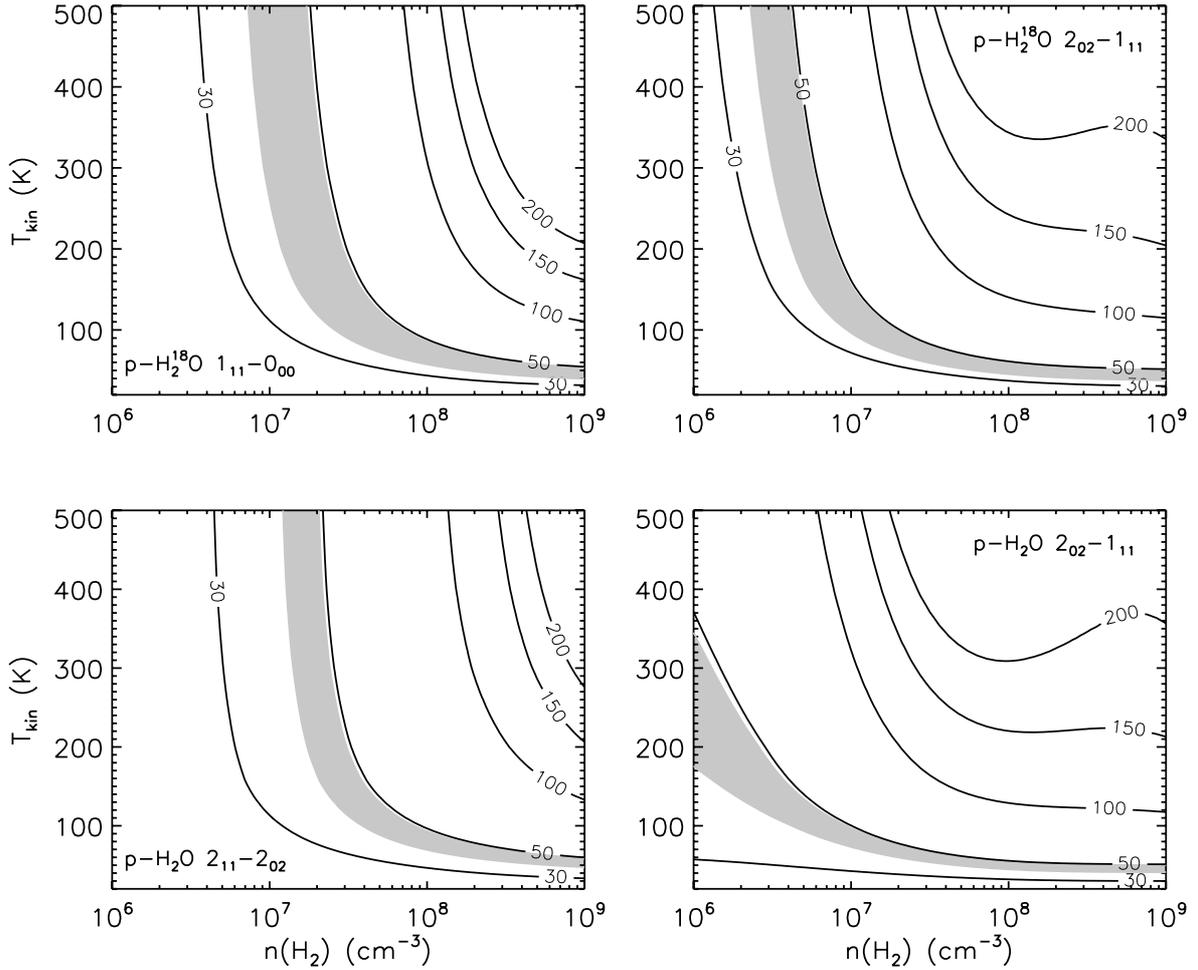
Fig. 5. Excitation temperature of p-$H_2^{18}O$ $1_{11}-0_{00}$, p-$H_2^{18}O$ $2_{02}-1_{11}$ for the envelope (*upper*) and the p-H_2O $2_{11}-2_{02}$, p-H_2O $2_{02}-1_{11}$ for the outflow (*lower*) assuming H_2O column densities of $N(H_2O) = 1 \times 10^{14}$ cm^{-2} and $N(H_2O) = 5 \times 10^{13}$ cm^{-2} and source sizes of 4″ and 30″ for the envelope and the outflow, respectively as a function of kinetic temperature and H_2 density calculated with RADEX (Non-LTE, large velocity gradient code). The gray areas indicate the derived T_{ex} of envelope and outflow from the LTE rotation diagram analysis.

Table 4. Physical conditions for each components.

Components	V_{LSR} (km s^{-1})	*FWHM* (km s^{-1})	$N(CO)$ (cm^{-2})	$N(H_2)$ (cm^{-2})	$N(H_2O)$ (cm^{-2})	$X(H_2O)$
Foreground[a]	0		$\gtrsim 3 \times 10^{17d}$	$\gtrsim 3 \times 10^{21}$	$\sim 5.2 \times 10^{13h}$	$\lesssim 1.7 \times 10^{-8}$
Weaker foreground[a]	+13		$\lesssim 6 \times 10^{15d}$	$\sim 8 \times 10^{20e} - 6 \times 10^{21}$	$\sim 1.6 \times 10^{12h}$	$\sim 2.7 \times 10^{-10} - 2 \times 10^{-9}$
Envelope[b]	-5.5	5–6	$\sim 10^{18d}$	$\sim 10^{22}$	$\sim 1.7 \times 10^{14i}$	1.7×10^{-8}
			7.2×10^{18f}	7.2×10^{22}		2.4×10^{-9}
			7.29×10^{18g}	2.7×10^{22}		6.3×10^{-9}
Outflow[c]	−10	10–11	1.5×10^{18d}	1.5×10^{22}	$\sim 4.2 \times 10^{13j}$	2.8×10^{-9}
			6.6×10^{18f}	6.6×10^{22}		6.4×10^{-10}

Notes. [a] V_{LSR} of two foreground components are from the p-H_2O $1_{11}-0_{00}$ line. [b] V_{LSR} and FWHM of the envelope component is from $H_2^{18}O$ lines. [c] V_{LSR} and FWHM of the outflow component is from broad components seen the p-H_2O $2_{02}-1_{11}$, p-H_2O $2_{11}-2_{02}$, and o-H_2O $3_{12}-3_{03}$ lines. [d] van der Wiel et al. (2013). [e] A lower limit from HF 1–0 observations. Emprechtinger et al. (2012). [f] Mitchell et al. (1989). [g] CO column density from $C^{18}O$ $J = 9-8$ observations assuming an abundance of $^{16}O/^{18}O$ of 540. San José-García et al. (2013). [h] The total (ortho+para) H_2O column density assuming an o/p ratio of 3. [i] H_2O column density for the envelope for a source size of 4″. [j] H_2O column density for the outflow for a source size of 30″.

the RADEX calculation as data points at different kinetic temperatures, T_{kin}, and densities, $n(H_2)$. We apply a molecular column density of $N(H_2O) = 5 \times 10^{13}$ cm^{-2} and a line width of 10.5 km s^{-1}. Figure 6 presents the rotation diagrams for the broad components of the three excited-state lines of

H_2O assuming a kinetic temperature of $T_{kin} = 100$ K as examples. Open circles are the data from the RADEX calculations. The overplotted line represents a linear fit to the rotational diagram. The rotation temperatures, T_{rot}, are below the input kinetic temperature of $T_{kin} = 100$ K. At higher H_2 density the rotation
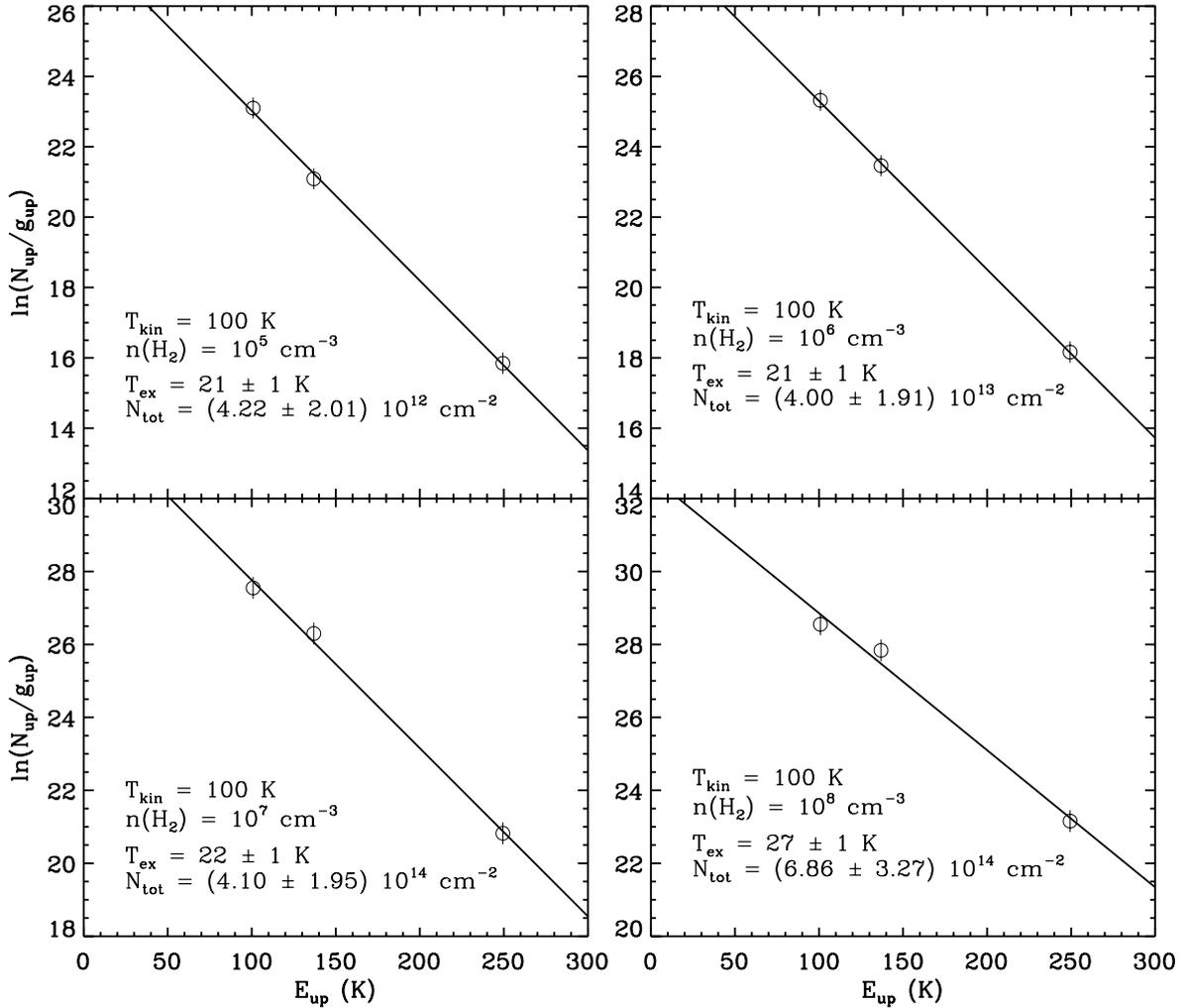
Fig. 6. Examples of rotation diagram for the p-H_2O $2_{02}-1_{11}$, p-H_2O $2_{11}-2_{02}$, and o-H_2O $3_{12}-3_{03}$ emission lines originating in the outflow at a given kinetic temperature of $T_{kin} = 100$ K from the RADEX calculations (non-LTE analysis). Open circles are the data from the non-LTE models. The overplotted line corresponds to a linear fit to the rotational diagram.

temperature is higher than at low H_2 density but our results show that the rotation temperature is well below the kinetic temperature, even at $n(H_2) = 10^8$ cm^{-3}. Higher densities are implausible for AFGL 2591 at the spatial scales probed by our data.

5. Discussion

We estimate the H_2O abundance in the various physical components of AFGL 2591 (Table 4) assuming a constant abundance for the protostellar envelope. First, van der Wiel et al. (2013) presents an absorption feature seen in CO 5–4 and JCMT data of CO 3–2 near 0 km s^{-1}, which is known to be a foreground component. They derived a column density $N(H_2) \gtrsim 3 \times 10^{21}$ cm^{-2} assuming an abundance of CO/H_2 of 10^{-4}. Assuming an o/p ratio of 3, we estimate the total (ortho+para) H_2O column density for the 0 km s^{-1} foreground component using the p-H_2O $1_{11}-0_{00}$ line. We find that the total H_2O column density is $\sim 5.2 \times 10^{13}$ cm^{-2}. and the abundance of H_2O is $\lesssim 1.7 \times 10^{-8}$, consistent with ion-molecule chemistry. In addition to the 0 km s^{-1} foreground component, there is another weak absorption component at 13 km s^{-1}, for which van der Wiel et al. (2013) obtained limits on the H_2 column density. As an upper limit, they estimated $N(H_2) \lesssim 6 \times 10^{21}$ cm^{-2} based on their ^{13}CO 1–0 spectrum. In addition, they used the HF 1–0

spectrum presented by Emprechtinger et al. (2012) to obtain a lower limit for the column density of the 13 km s^{-1} foreground component. They found that $N(H_2) \gtrsim 8 \times 10^{20}$ cm^{-2} assuming HF/H_2 = 3.6×10^{-8}. We estimate the H_2O column density of $N(H_2O) = 1.6 \times 10^{12}$ cm^{-2} using the p-H_2O $1_{11}-0_{00}$ line under the assumptions that an o/p ratio is 3, so that the H_2O abundance in this component is $\sim 10^{-9}$. This lower abundance compared with the 0 km s^{-1} component is consistent with enhanced photodissociation in diffuse gas.

In order to derive the H_2O abundance in the outflow and envelope components, we use two methods to estimate the H_2 column density. We adopt the H_2O column densities of $\sim 1.7 \times 10^{14}$ cm^{-2} for the envelope and $\sim 4.2 \times 10^{13}$ cm^{-2} for the outflow, in source sizes of 4″ and 30″, respectively, based on LTE calculations. Mitchell et al. (1989) detected CO and ^{13}CO rovibrational absorption lines near 4.7 μm and found a cold ($\sim$38 K) and a hot ($\sim$1000 K) component in the quiescent gas centered around -5 km s^{-1}, and a blueshifted warm ($\sim$200 K) component. The cold component is likely the outer envelope of AFGL 2591, while the hot gas is near the infrared source and is heated by its luminosity. Despite their different temperatures, the CO column densities of the three components are all in the range 5–7 $\times 10^{18}$ cm^{-2}. We use the column density from the cold gas for the envelope, and that of the blueshifted warm gas

for the outflow, and derive the column density of H_2 using a ratio $N(^{12}CO)/N(H_2) = 10^{-4}$. We find that the abundance of H_2O is 2.4×10^{-9} for the envelope and 6.4×10^{-10} for the outflow.

As a second method, we estimate $N(H_2)$ from submillimeter observations. San José-García et al. (2013) presented *Herschel*/HIFI observations of high-*J* CO and isotopologues from low-to high-mass star-forming regions. They estimated a H_2 column density for AFGL 2591 of 2.7×10^{22} cm^{-2} in a ∼20″ beam using C^{18}O $J = 9$–8 for an excitation temperature of 75 K. Using this column density of H_2, we find that the abundance of H_2O is 6.3×10^{-9} for the envelope in a source size of 4″. van der Wiel et al. (2013) also estimated the column density of H_2 for the envelope and outflow regions using *Herschel*/HIFI data of CO and they found that the column density of H_2 is ∼10^{22} cm^{-2} and 1.5×10^{22} cm^{-2} for the envelope and outflow, respectively. Using these numbers, the abundance of H_2O is 1.7×10^{-8} for the envelope and 2.8×10^{-9} for the outflow. Since our derived H_2O source size of 4″ is between the beam sizes of the infrared and submillimeter estimates for $N(H_2)$, the most likely value for the H_2O abundance is between the above estimates. Since the outflow gas is more extended, the abundance estimate from the submillimeter CO data is probably the best.

In summary, our *Herschel*/HIFI observations indicate water abundances of ∼2×10^{-9}–2×10^{-8} and a kinetic temperature of ∼60–230 K in the envelope. These abundances are much lower than found from infrared (ISO) data (Sect. 1), which indicates that our observed emission comes mostly from the cold outer envelope. Indeed, our derived water abundance is similar to the values of 5×10^{-10} to 4×10^{-8} found for the outer envelopes of other high-mass protostars (van der Tak et al. 2010; Chavarría et al. 2010; Marseille et al. 2010; Herpin et al. 2012), and also for low-mass protostellar envelopes (Kristensen et al. 2012). In contrast, the infrared absorption data are mostly sensitive to the warm inner envelope, and we expect this gas to emit primarily in the PACS lines rather than the HIFI lines. Indeed, using the *Herschel*/PACS instrument, Karska et al. (2014) probe a warm water component which is similar to the gas seen with ISO.

For the outflow, we find a water abundance of ∼6×10^{-10}–3×10^{-9} and a kinetic temperature of ∼70–90 K. Despite the similar temperatures, the H_2O abundance in the outflow is a factor of 10 lower than in the AFGL 2591 envelope and also lower than found for other outflows, both from high-mass (van der Tak et al. 2010; Emprechtinger et al. 2013) and low-mass (Bjerkeli et al. 2012) protostars. The abundance estimate is uncertain through the adopted source size, but this effect is probably small as seen from a comparison of the column densities measured in absorption (Table 3) and emission (Table 4). The absorbing column is almost twice the emitting column, which suggests a source size of ∼20″ rather than ∼30″, assuming that the features arise in the same gas. The corresponding effect on the H_2O column density and abundance is only a factor of 2. However, the effect is probably smaller because the emission occurs over a smaller velocity range (from -15 to -5 km s^{-1}) than the absorption (from -24 to -5.5 km s^{-1}) which suggests that the features do not arise in the same gas. More likely, the water in the outflow lobes is affected by dissociating UV radiation, which also means that the $H_2^{18}O$ lines are dominated by shocks at the interface between the jets and the envelope.

6. Conclusions

1. We present 14 rotational transitions of H_2O, $H_2^{17}O$, and $H_2^{18}O$ toward the massive star-forming region AFGL 2591.

2. We find redshifted water absorption from cold foreground clouds and blueshifted absorption from the outflow. Similar line features are found in W3 IRS5 (Chavarría et al. 2010) and DR21 (van der Tak et al. 2010)

3. We derived the o/p ratio using the ground-state lines of the main isotopologue and found that the o/p ratio is ∼2 in the cold foreground cloud, while the o/p ratio is ∼3 in the warm protostellar envelope. Similar results are found toward Sgr B2(M) (Lis et al. 2010) and NGC 6334 I (Emprechtinger et al. 2010). The inferred water abundances in the foreground clouds are consistent with ion-molecule chemistry.

4. Radiative transfer models indicate that the envelope of AFGL 2591 is warm ($T_{kin} \sim 60$–230 K). However, the low derived H_2O abundance (∼2×10^{-9}–2×10^{-8}) suggests that the H_2O line emission is dominated by the cold outer envelope where freeze-out of water onto dust grains is important. This apparent contradiction suggests that the water abundance in the protostellar envelope varies with radius.

5. The water abundance in the outflow is ∼10× lower than in the envelope and in the outflows of other high- and low-mass protostars. Part of this difference may be due to beam size effect, but another possibility is the effect of dissociating UV radiation (van Dishoeck et al. 2013). Compared to the envelope, the outflow lobes have a lower extinction, which leads to a higher UV radiation field and thus more rapid photodissociation. However, why this outflow has a lower H_2O abundance than those of other high-mass protostars is unclear. Models of UV-irradiated shocks are being developed to interpret the observed water abundances in protostellar outflows (Kaufman, priv. comm.).

The environment of AFGL 2591 has been the target of many observations from the ground and from space, but the *Herschel*/HIFI H_2O observations show the kinematics of this source (outflow, expanding envelope, foreground cloud) in more detail than any previous study. This opportunity will be further explored with detailed radiative transfer models (Hogerheijde & van der Tak 2000) in a future paper, where we will estimate H_2O abundance profiles for a sample of high-mass protostellar envelopes.

Appendix A: RADEX line ratio plot

In Sects. 4.3 we calculate the line ratios of p-H_2O 2_{11}–2_{02} and p-H_2O 2_{02}–1_{11} using the non-LTE code RADEX (van der Tak et al. 2007). Figure A.1 shows the p-H_2O 2_{11}–2_{02} and p-H_2O 2_{02}–1_{11} line intensity ratio for kinetic temperatures between 20 K and 300 K and H_2 densities between 10^3 cm^{-3} and 5×10^8 cm^{-3}.
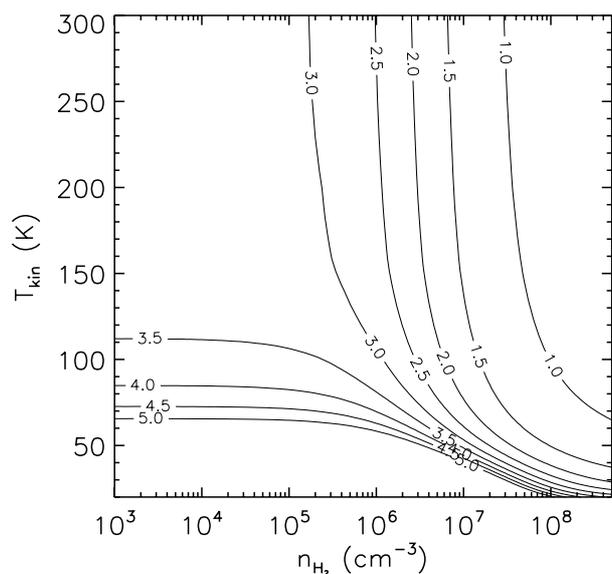
Fig. A.1. Line ratios of p-H_2O $2_{11}-2_{02}$ and p-H_2O $2_{02}-1_{11}$ as a function of kinetic temperature and H_2 density.

References

Bjerkeli, P., Liseau, R., Larsson, B., et al. 2012, A&A, 546, A29
Blake, G. A., Sutton, E. C., Masson, C. R., et al. 1984, ApJ, 286, 586
Blake, G. A., Sutton, E. C., Masson, C. R., & Phillips, T. G. 1987, ApJ, 315, 621
Boonman, A. M. S., Doty, S. D., van Dishoeck, E. F., et al. 2003, A&A, 406, 937
Chavarría, L., Herpin, F., Jacq, T., et al. 2010, A&A, 521, L37
Daniel, F., Dubernet, M.-L., & Grosjean, A. 2011, A&A, 536, A76
de Graauw, T., Helmich, F. P., Phillips, T. G., et al. 2010, A&A, 518, L6
Emprechtinger, M., Lis, D. C., Bell, T., et al. 2010, A&A, 521, L28
Emprechtinger, M., Monje, R. R., van der Tak, F. F. S., et al. 2012, ApJ, 756, 136
Emprechtinger, M., Lis, D. C., Rolffs, R., et al. 2013, ApJ, 765, 61
Flagey, N., Goldsmith, P. F., Lis, D. C., et al. 2013, ApJ, 762, 11
Goldsmith, P. F., & Langer, W. D. 1999, ApJ, 517, 209
Helmich, F. P., Jansen, D. J., de Graauw, T., Groesbeck, T. D., & van Dishoeck, E. F. 1994, A&A, 283, 626
Helmich, F. P., van Dishoeck, E. F., Black, J. H., et al. 1996, A&A, 315, L173
Herpin, F., Chavarría, L., van der Tak, F., et al. 2012, A&A, 542, A76
Hogerheijde, M. R., & van der Tak, F. F. S. 2000, A&A, 362, 697
Karska, A., Herpin, F., Bruderer, S., et al. 2014, A&A, 562, A45
Kristensen, L. E., Visser, R., van Dishoeck, E. F., et al. 2010, A&A, 521, L30
Kristensen, L. E., van Dishoeck, E. F., Bergin, E. A., et al. 2012, A&A, 542, A8
Lada, C. J., Thronson, Jr., H. A., Smith, H. A., Schwartz, P. R., & Glaccum, W. 1984, ApJ, 286, 302
Linke, R. A., Frerking, M. A., & Thaddeus, P. 1979, ApJ, 234, L139
Lis, D. C., Phillips, T. G., Goldsmith, P. F., et al. 2010, A&A, 521, L26
Marseille, M. G., van der Tak, F. F. S., Herpin, F., et al. 2010, A&A, 521, L32
Mitchell, G. F., Curry, C., Maillard, J.-P., & Allen, M. 1989, ApJ, 341, 1020
Mumma, M. J., Weaver, H. A., & Larson, H. P. 1987, A&A, 187, 419
Ott, S. 2010, in Astronomical Data Analysis Software and Systems XIX, eds. Y. Mizumoto, K.-I. Morita, & M. Ohishi, ASP Conf. Ser., 434, 139
Pilbratt, G. L., Riedinger, J. R., Passvogel, T., et al. 2010, A&A, 518, L1
Roelfsema, P. R., Helmich, F. P., Teyssier, D., et al. 2012, A&A, 537, A17
Rygl, K. L. J., Brunthaler, A., Sanna, A., et al. 2012, A&A, 539, A79
San José-García, I., Mottram, J. C., Kristensen, L. E., et al. 2013, A&A, 553, A125
Sanna, A., Reid, M. J., Carrasco-González, C., et al. 2012, ApJ, 745, 191
Schöier, F. L., van der Tak, F. F. S., van Dishoeck, E. F., & Black, J. H. 2005, A&A, 432, 369
van der Tak, F. F. S., van Dishoeck, E. F., Evans, II, N. J., Bakker, E. J., & Blake, G. A. 1999, ApJ, 522, 991
van der Tak, F. F. S., Walmsley, C. M., Herpin, F., & Ceccarelli, C. 2006, A&A, 447, 1011
van der Tak, F. F. S., Black, J. H., Schöier, F. L., Jansen, D. J., & van Dishoeck, E. F. 2007, A&A, 468, 627
van der Tak, F. F. S., Marseille, M. G., Herpin, F., et al. 2010, A&A, 518, L107
van der Wiel, M. H. D., Pagani, L., van der Tak, F. F. S., Kaźmierczak, M., & Ceccarelli, C. 2013, A&A, 553, A11
van Dishoeck, E. F., Kristensen, L. E., Benz, A. O., et al. 2011, PASP, 123, 138
van Dishoeck, E. F., Herbst, E., & Neufeld, D. A. 2013, Chem. Rev., 113, 9043
Wang, K.-S., van der Tak, F. F. S., & Hogerheijde, M. R. 2012, A&A, 543, A22
Wilson, T. L., & Rood, R. 1994, ARA&A, 32, 191